Failsafe flux limiting and constrained data projections for systems of conservation laws

Dmitri Kuzmin [a] Matthias Möller [b] John N. Shadid [c]
Mikhail Shashkov [d]

[a] *Department of Mathematics, University of Houston, 651 Philip G. Hoffman Hall, Houston, TX 77204-3008, USA*

[b] *Institute of Applied Mathematics (LS III), Dortmund University of Technology, Vogelpothsweg 87, D-44227, Dortmund, Germany*

[c] *Computational Sciences R&D Group, Sandia National Laboratories, PO Box 5800 MS 0316, Albuquerque, NM 87185-0316, USA*

[d] *Los Alamos National Laboratory, Theoretical Division, T-5, MS B284, Los Alamos, NM 87545, USA*

Abstract

A new approach to flux limiting for systems of conservation laws is presented. The Galerkin finite element discretization / L^2 projection is equipped with a failsafe mechanism that prevents the birth and growth of spurious local extrema. Within the framework of a synchronized flux-corrected transport (FCT) algorithm, the velocity and pressure fields are constrained using node-by-node transformations from the conservative to the primitive variables. An additional correction step is included to ensure that all the quantities of interest (density, velocity, pressure) are bounded by the physically admissible low-order values. The result is a conservative and bounded scheme with low numerical diffusion. The new failsafe FCT limiter is integrated into a high-resolution finite element scheme for the Euler equations of gas dynamics. Also, bounded L^2 projection operators for conservative interpolation/initialization are designed. The performance of the proposed limiting strategy and the need for a posteriori control of flux-corrected solutions are illustrated by numerical examples.

Key words: systems of conservation laws, finite elements, maximum principle, flux-corrected transport, local extremum diminishing interpolation

PACS: 02.60.Cb, 02.70.Dh, 47.11.Fg

Email addresses: kuzmin@math.uh.edu (Dmitri Kuzmin), matthias.moeller@math.tu-dortmund.de (Matthias Möller), jnshadi@sandia.gov (John N. Shadid), shashkov@lanl.gov (Mikhail Shashkov).

1 Introduction

The development of the *flux-corrected transport* (FCT) algorithm [3,25] in the 1970s was an important milestone for numerical simulation of fluid flows. During the past decades, flux limiting has become a popular approach to enforcing monotonicity constraints in modern high-resolution schemes for (systems of) conservation laws [12–14,19,25]. The idea behind the classical FCT method is remarkably simple. First, the difference between conservative approximations of high and low order is decomposed into a sum of antidiffusive fluxes. Next, each flux is multiplied by a solution-dependent correction factor, that was determined by a flux limiter, and this limited flux is added to the low-order solution. The purpose of the flux limiter is to ensure that no new maxima or minima can form, and existing extrema cannot grow. That is, the limited antidiffusive correction must be *local extremum diminishing* (LED).

The LED criterion turns out to be a powerful and versatile tool when it comes to the design of numerical advection schemes as well as constrained data projection (initialization, interpolation, remapping) techniques. The first use of FCT in the latter context dates back to the work of Váchal and Liska [22], Löhner [14], and Shashkov et al. [13]. Another notable contribution to the field is the recent paper by Farrell et al. [5] who present a bounded L^2 projection operator for globally conservative interpolation between unstructured meshes. In all of the above applications, the challenge is to enforce the local discrete maximum principle (positivity, monotonicity, or the LED property) in a conservative manner and minimize the amount of numerical diffusion.

A major bottleneck in the development of FCT limiters for systems of conservation laws, including the Euler and Navier-Stokes equations of fluid dynamics, is the intricate coupling between the quantities of interest. In conservative numerical schemes, the primary unknowns are the density, momentum, and total energy. However, a limiter designed to control the local maxima and minima of the conserved quantities does not guarantee that the pressure or internal energy will stay nonnegative. Likewise, the velocity is not directly constrained and may exhibit spurious fluctuations. Since the rate of transport depends on the spiky velocity and pressure fields, undershoots and overshoots eventually carry over to the conservative variables. As a typical consequence, the speed of sound becomes negative, indicating that the simulation is going to crash.

Limiters that constrain the primitive (density, velocity, pressure) or characteristic variables are typically more reliable but the involved linearizations may also cause them to fail, no matter how carefully they are designed. While it is impossible to rule out the formation of spurious maxima/minima a priori, they can be easily detected and removed at a postprocessing step. This philosophy was recently embraced by Zalesak [26] who used it to maintain the nonneg-

ativity of pressures and internal energies in a characteristic FCT method for the compressible Euler equations. The failsafe corrector to be presented below is a generalization of Zalesak's idea. Instead of enforcing global constraints (such as nonnegativity), it guarantees that the flux correction step is local extremum diminishing for a given set of control variables. Whenever the added antidiffusive flux is found to create an undershoot or overshoot, the numerical solution is 'repaired' by removing (a certain portion of) the offending flux.

In classical FCT algorithms for systems [14–16], the conversion between the conservative and primitive variables is performed edge-by-edge using linearizations about an intermediate state associated with each pair of nodes. In our experience, averaging across shocks and contact discontinuities may give rise to unbounded solutions in particularly sensitive compressible flow problems. Therefore, we propose a primitive variable FCT limiter featuring a node-based linearization procedure. The advantages of this approach are twofold. First, the transformation matrix is the same for all antidiffusive fluxes into a given node. Second, the upper and lower bounds for FCT are the exact low-order nodal values of the primitive variables. This makes the limiting procedure very robust, so that the need for a failsafe repair of the final solution is rare. Last but not least, a node-based transformation to the primitive variables requires fewer arithmetic operations than an edge-based linearization procedure.

In this paper, we apply the failsafe FCT limiter to a finite element discretization of the compressible Euler equations. Also, we develop an FCT-constrained L^2 projection scheme for conservative initialization/interpolation of data. The presented numerical examples demonstrate that the proposed limiting strategy is well suited for applications that involve simultaneous transport/projection of mass, momentum, and energy in the presence of strong discontinuities.

2 Flux decomposition and limiting

In a typical system of conservation laws, the vector of unknowns is given by

$$U = [\rho, \rho\mathbf{v}, \rho E]^T,$$

where ρ is the density, $\mathbf{v}$ is the velocity field, and E is the total energy. These variables are related to the pressure p by an equation of state. In the case of an ideal polytropic gas with a constant ratio of specific heats γ, we have

$$p = (\gamma - 1)\rho\left(E - \frac{|\mathbf{v}|^2}{2}\right). \tag{1}$$

After the discretization in space, the numerical solution U_h is defined by a finite number of time-dependent nodal values $\{U_i\}$. Depending on the method of approximation (finite differences, finite volumes, finite elements), they may represent the values of U_h at the vertices of the mesh, control volume averages, or the coefficients of piecewise-polynomial basis functions denoted by $\{\varphi_i\}$.

In this paper, we are concerned with constraining the difference between a low-order approximation U_i^L and its high-order counterpart U_i^H. The former is assumed to be inaccurate but free of spurious local extrema. The latter is usually well-resolved in regions of smoothness but may contain undershoots or overshoots in proximity to shocks, contact discontinuities, and steep fronts.

Furthermore, the difference between the nodal values U_i^H and U_i^L must admit a conservative decomposition into a sum of numerical fluxes. Suppose that

$$m_i U_i^H = m_i U_i^L + \sum_{j \neq i} F_{ij}, \qquad F_{ji} = -F_{ij}. \tag{2}$$

In finite difference and finite volume schemes, the coefficient m_i is defined as the volume/area of the i-th cell in the dual mesh. In finite element methods, m_i is the i-th diagonal entry of the lumped mass matrix (see Section 6).

The flux F_{ij} is antidiffusive in nature and has the same size as U. That is,

$$F_{ij} = [f_{ij}^{\rho}, \mathbf{f}_{ij}^{\rho v}, f_{ij}^{\rho E}]^T. \tag{3}$$

Since F_{ji} has the same magnitude and opposite sign, all fluxes cancel upon summation. Hence, the solutions U^H and U^L have the same total 'mass'

$$\sum_i m_i U_i^H = \sum_i m_i U_i^L.$$

Moreover, it is possible to adjust the magnitude of each flux pair without changing the mass balance. The simplest way to enforce monotonicity is to multiply all components of F_{ij} by a solution-dependent correction factor α_{ij}. The result is a nonlinear blend of the high- and low-order approximations

$$m_i U_i = m_i U_i^L + \sum_{j \neq i} \alpha_{ij} F_{ij}, \qquad \alpha_{ji} = \alpha_{ij}. \tag{4}$$

The definition of $\alpha_{ij} \in [0, 1]$ must guarantee that not only the conservative variables but also certain derived quantities (e.g., velocity, pressure, and internal energy) will stay bounded by the local maxima and minima of the nonoscillatory low-order solution. In what follows, we discuss some new ideas concerning the computation of α_{ij} for systems of conservation laws. The methodology

to be presented represents a generalization of the classical FCT algorithms developed by Boris and Book [3], Zalesak [25,26], and Löhner et al. [14,16].

3 Transformation to primitive variables

The design of FCT algorithms for systems is more difficult than that for scalar conservation laws. If the density, momentum, and energy increments are limited separately, the strong coupling may give rise to undershoots/overshoots in all quantities of interest. The remedies to this problem include [12,15,26]

- synchronization of the correction factors for selected control variables;
- transformations to nonconservative variables (primitive, characteristic);
- a posteriori control and postprocessing of the flux-corrected solution.

In the context of FCT, "synchronization" means using the same value of α_{ij} for all fields, as in (4). This strategy is to be recommended whenever the variables to be limited are strongly coupled [12,16,15]. The transformation to local characteristic variables decouples the antidiffusive fluxes and eliminates the need for synchronization [26]. However, flux correction in terms of characteristic variables is expensive and requires dimensional splitting in 2D/3D.

The objective of the present paper is to design a synchronized FCT limiter for the primitive variables (density ρ, velocity $\mathbf{v}$, and pressure p). Let

$$\mathbf{v}_i = \frac{(\rho\mathbf{v})_i}{\rho_i}, \qquad p_i = (\gamma - 1)\left[(\rho E)_i - \frac{|(\rho\mathbf{v})_i|^2}{2\rho_i}\right]. \tag{5}$$

The computation of the synchronized correction factor α_{ij} for the contribution of the raw antidiffusive flux F_{ij} to the right-hand side of (4) involves the following transformations of the increments to be limited (see [8], Chapter 16)

$$\mathbf{f}_{ij}^v = \frac{\mathbf{f}_{ij}^{\rho v} - \mathbf{v}_i f_{ij}^\rho}{\rho_i}, \qquad f_{ij}^p = (\gamma - 1)\left[\frac{|\mathbf{v}_i|^2}{2} f_{ij}^\rho - \mathbf{v}_i \cdot \mathbf{f}_{ij}^{\rho v} + f_{ij}^{\rho E}\right]. \tag{6}$$

Note that the velocity and pressure 'fluxes' are generally not skew-symmetric

$$\mathbf{f}_{ji}^v \neq -\mathbf{f}_{ij}^v, \qquad f_{ji}^p \neq -f_{ij}^p.$$

It is neither necessary nor desirable to preserve the skew-symmetry of antidiffusive fluxes after the transformation to nonconservative variables. As explained in the next section, the transformed 'fluxes' are only needed to determine the value of the correction factor α_{ij} for the conservative solution update (4).

4 Synchronized FCT limiter

To begin with, we present a generalization of Zalesak's multidimensional FCT limiter [25,26] for a single control variable. Let u_i^L be the low-order approximation to ρ, v, or p. The antidiffusive 'flux' from node j into node i is denoted by f_{ij}^u. The conversion to the primitive variables is based on (5) and (6).

In accordance with the original FCT philosophy, the choice of the correction factors α_{ij}^u must ensure that the limited antidiffusive correction of u_i^L is local extremum diminishing. Mathematically speaking, we require [11]

$$m_i(u_i^{\min} - u_i^L) \le \sum_{j\neq i} \alpha_{ij}^u f_{ij}^u \le m_i(u_i^{\max} - u_i^L), \tag{7}$$

where $u_i^{\max}$ and $u_i^{\min}$ are the maxima and minima of the low-order solution

$$u_i^{\max} - u_i^L = \max_{j\neq i}(u_j^L - u_i^L), \qquad u_i^{\min} - u_i^L = \min_{j\neq i}(u_j^L - u_i^L). \tag{8}$$

Of course, the index set "$j \neq i$" contains the nearest neighbors of node i only.

The next step is the calculation of correction factors α_{ij}^u satisfying (7) for the given data. This task involves the following algorithmic steps (cf. [11,25]):

(1) Compute the sums of positive/negative antidiffusive increments to node i

$$P_i^+ = \sum_{j\neq i} \max\{0, f_{ij}^u\}, \qquad P_i^- = \sum_{j\neq i} \min\{0, f_{ij}^u\}. \tag{9}$$

(2) Compute the distance to a local extremum of the low-order predictor

$$Q_i^+ = u_i^{\max} - u_i^L, \qquad Q_i^- = u_i^{\min} - u_i^L. \tag{10}$$

(3) Compute the nodal correction factors for the net increment to node i

$$R_i^+ = \min\left\{1, m_i Q_i^+ / P_i^+\right\}, \qquad R_i^- = \min\left\{1, m_i Q_i^- / P_i^-\right\}. \tag{11}$$

(4) Define $\alpha_{ij}^u = \alpha_{ji}^u$ so as to satisfy the FCT constraints for nodes i and j

$$\alpha_{ij}^u = \min\{R_{ij}, R_{ji}\}, \qquad R_{ij} = \begin{cases} R_i^+, & \text{if } f_{ij}^u \ge 0, \\ R_i^-, & \text{if } f_{ij}^u < 0. \end{cases} \tag{12}$$

(5) Apply α_{ij}^u to all components of the raw antidiffusive flux given by (3).

This generalization of Zalesak's FCT limiter to the case of $f_{ji}^u \neq -f_{ij}^u$ can be used to control selected quantities (typically, the pressure and/or density) or

all primitive variables. In the latter case, the synchronized correction factor α_{ij} for the constrained solution update (4) can be defined as [12,16,15]

$$\alpha_{ij} = \min\{\alpha_{ij}^{\rho}, \alpha_{ij}^{v}, \alpha_{ij}^{p}\}. \tag{13}$$

Alternatively, one can apply the pressure limiter to the density-limited fluxes and pass the result to the velocity limiter. This sequential version yields

$$\alpha_{ij} = \alpha_{ij}^{v}\alpha_{ij}^{p}\alpha_{ij}^{\rho}, \tag{14}$$

where α_{ij}^{ρ} constrains F_{ij}, α_{ij}^{p} constrains $\alpha_{ij}^{\rho}F_{ij}$, and α_{ij}^{v} constrains $\alpha_{ij}^{p}\alpha_{ij}^{\rho}F_{ij}$.

In contrast to (13), the final value of α_{ij} depends on the order in which the single-field correction factors α_{ij}^{u} are calculated. However, the raw antidiffusive increments f_{ij}^{u} already include the net effect of previous corrections. Thus, only fluxes that still violate the FCT design criterion (7) need to be constrained.

In the multidimensional case, the velocity correction factor α_{ij}^{v} can be defined as a linear combination of $\alpha_{ij}^{(d)},\ d = 1, 2, 3$ calculated independently for each velocity component $v^{(d)}$. Let $\mathbf{v}_{ij} = \frac{1}{2}(\mathbf{v}_i + \mathbf{v}_j)$ be the mean edge velocity and

$$\alpha_{ij}^{v} = \sum_{d=1}^{3} \left(\frac{v_{ij}^{(d)}}{|\mathbf{v}_{ij}|} \right)^2 \alpha_{ij}^{(d)}. \tag{15}$$

The numerical results to be presented in Section 7 were calculated with (14) and (15) since synchronization of the form (13) is generally more diffusive.

5 Failsafe flux correction

Since the transformation of variables in (5) and (6) involves a linearization about the low-order solution at node i, there is no guarantee that the flux-corrected solution given by (4) will stay within the original bounds, especially in the presence of large jumps. Therefore, our limiting strategy includes a postprocessing step in which all undershoots and overshoots are detected and removed. The first 'failsafe' flux limiter of this kind was proposed by Zalesak (see [26], pp. 36 and 56). His recipe is very simple: "if, after flux limiting, either the density or the pressure in a cell is negative, all the fluxes into that cell are set to their low order values, and the grid point values are recalculated." It is tacitly assumed that the low-order solution is free of nonphysical values.

In the present paper, we propose a similar approach to enforcing **local** FCT constraints in a failsafe manner. Let u_i denote the flux-corrected value of the control variable u at node i. It is regarded as acceptable whenever

$$u_i^{\min} \le u_i \le u_i^{\max}. \tag{16}$$

As before, $u_i^{\max}$ and $u_i^{\min}$ are the local extrema of the low-order solution u^L. If any quantity of interest (density, velocity, pressure) has an undershoot/overshoot at node i, then a fixed percentage of the added antidiffusive fluxes $\alpha_{ij}F_{ij}$ and $\alpha_{ji}F_{ji}$ is removed until the offense is eliminated. In the N-step version of our failsafe limiter, the difference between the unacceptable nodal value U_i and the low-order predictor U_i^L is gradually reduced as follows:

$$m_i U_i^{(m)} = m_i U_i - \sum_{j\neq i} \beta_{ij}^{(m)} (\alpha_{ij} F_{ij}), \qquad m = 1, \ldots, N. \tag{17}$$

If the (selected) primitive variables satisfy (16), and a similar constraint holds for node j, then we set $\beta_{ij}^{(m)} = \beta_{ij}^{(m-1)}$ with $\beta_{ij}^{(0)} = 0$. Otherwise, the added antidiffusion is reduced by the factor $\beta_{ij}^{(m)} = m/N$. If the undershoot/overshoot still exists at the last correction cycle, the final result is $U_i^{(N)} = U_i^L$.

The number of correction cycles N depends on the effort invested in the calculation of α_{ij}. If the synchronized FCT limiter is applied to all primitive variables, then undershoots and overshoots are an exception, so that $N = 1$ is optimal. On the other hand, 3-5 cycles may be appropriate if $\alpha_{ij} = \alpha_{ij}^{\rho}$ or $\alpha_{ij} = \alpha_{ij}^{p}$. The choice of N affects only the amount of rejected antidiffusion. The bounds of the low-order solution are guaranteed to be preserved even for $\alpha_{ij} \equiv 1$. Hence, the failsafe corrector can not only reinforce but also replace the synchronized FCT limiter, as shown by the numerical examples below.

REMARK. In practice, failsafe flux correction based on (16) may give rise to unnecessary limiting, e.g., at contact discontinuities where the density has a jump but the velocity and pressure are constant. To avoid this, we relax (16) and require that $u_i^{\min} - \epsilon \le u_i \le u_i^{\max} + \epsilon$ for a prescribed tolerance $\epsilon > 0$.

6 Case study: the Euler equations

In this section, we define the raw antidiffusive fluxes F_{ij} for a FEM-FCT discretization of the Euler equations written in the generic divergence form in which the dot product implies summation over all space dimensions

$$\frac{\partial U}{\partial t} + \nabla \cdot \mathbf{F}(U) = 0 \qquad \text{in } \Omega. \tag{18}$$

This is a nonlinear hyperbolic system with $U = [\rho, \rho\mathbf{v}, \rho E]^T$. Remarkably, the relationship between the fluxes $\mathbf{F}$ and Jacobians $\mathbf{A} = \frac{\partial \mathbf{F}}{\partial U}$ is quasi-linear

$$\mathbf{F}(U) = \{\rho\mathbf{v}, \rho\mathbf{v} \otimes \mathbf{v} + p\mathcal{I}, (\rho E + p)\mathbf{v}\} = \mathbf{A}(U)U, \tag{19}$$

where $\mathcal{I}$ is the identity tensor. The formula for $\mathbf{A}$ can be found, e.g., in [8,12].

Within the framework of the group finite formulation [6,12], the approximate solution $U_h \approx U$ and the numerical flux function $\mathbf{F}_h \approx \mathbf{F}$ are interpolated using the same set of piecewise-polynomial basis functions $\{\varphi_i\}$. That is,

$$U_h = \sum_j U_j \varphi_j, \qquad \mathbf{F}_h = \sum_j \mathbf{F}_j \varphi_j, \tag{20}$$

where $\mathbf{F}_j = \mathbf{A}_j U_j$ due to the homogeneity property (19) of the Euler equations.

Inserting approximations (20) into the Galerkin weak form of (18), one obtains

$$\sum_j \left(m_{ij} \frac{\mathrm{d}U_j}{\mathrm{d}t} \right) = -\sum_j \mathbf{c}_{ij} \cdot \mathbf{F}_j = -\sum_j (\mathbf{c}_{ij} \cdot \mathbf{A}_j) U_j. \tag{21}$$

The coefficients of the consistent mass matrix $M_C = \{m_{ij}\}$ and those of the discrete gradient/divergence operator $\mathbf{C} = \{\mathbf{c}_{ij}\}$ are given by [11,12]

$$m_{ij} = \int_\Omega \varphi_i \varphi_j \, \mathrm{d}\mathbf{x}, \qquad \mathbf{c}_{ij} = \int_\Omega \varphi_i \nabla \varphi_j \, \mathrm{d}\mathbf{x}. \tag{22}$$

The nonoscillatory low-order discretization associated with (21) is constructed by adding a suitably designed artificial viscosity operator. Furthermore, the consistent mass matrix M_C is replaced by its lumped counterpart

$$M_L = \mathrm{diag}\{m_i\}, \qquad m_i = \int_\Omega \varphi_i \, \mathrm{d}\mathbf{x} = \sum_j m_{ij}. \tag{23}$$

After these manipulations, the semi-discrete equation for node i becomes

$$m_i \frac{\mathrm{d}U_i}{\mathrm{d}t} = -\sum_j (\mathbf{c}_{ij} \cdot \mathbf{A}_j) U_j + \sum_{j \neq i} D_{ij} (U_j - U_i). \tag{24}$$

In our multidimensional generalization [10,12] of Roe's approximate Riemann solver [18], the blocks D_{ij} of the artificial diffusion operator are designed using

a characteristic factorization of the cumulative Roe matrix A_{ij} satisfying

$$A_{ij}(U_j - U_i) = \frac{\mathbf{c}_{ji} - \mathbf{c}_{ij}}{2} \cdot (\mathbf{F}_j - \mathbf{F}_i).$$

The analytical derivation of A_{ij} involves the evaluation of the Jacobian $\mathbf{A}(U)$ for a special average of U_i and U_j [18]. The artificial viscosity operator can also be approximated by linearizing about the arithmetic mean edge state

$$A_{ij} = \frac{\mathbf{c}_{ji} - \mathbf{c}_{ij}}{2} \cdot \mathbf{A}\left(\frac{U_j + U_i}{2}\right).$$

Banks et al. [2] present a numerical study of methods that use this linearization. In particular, the expected order of accuracy is verified numerically.

In any event, the hyperbolicity of the Euler equations implies that

$$A_{ij} = R_{ij}\Lambda_{ij}R_{ij}^{-1},$$

where Λ_{ij} is the diagonal matrix of eigenvalues and R_{ij} is the matrix of right eigenvectors. To eliminate all negative eigenvalues of A_{ij}, we define [10,12]

$$D_{ij} = R_{ij}|\Lambda_{ij}|R_{ij}^{-1}. \tag{25}$$

In particularly sensitive applications, the so-defined minimum artificial viscosity may fail to suppress spurious oscillations. This is unacceptable since the flux limiting machinery relies on the assumption that the local extrema of the low-order solution constitute physically legitimate upper and lower bounds.

A more diffusive low-order scheme can be constructed using Rusanov-like scalar dissipation proportional to the maximum characteristic speed [2,26]. The following simple formula is likely to work when everything else fails

$$D_{ij} = \max\{d_{ij}, d_{ji}\}I, \qquad d_{ij} = |\mathbf{c}_{ij} \cdot \mathbf{v}_j| + |\mathbf{c}_{ij}|c_j, \tag{26}$$

where $c_i = \sqrt{\gamma p_i/\rho_i}$ is the local speed of sound, and I is the identity matrix with dimensions equal to those of A_{ij}. In implicit FEM-FCT schemes, this sort of scalar dissipation can be used for preconditioning purposes even if Roe's tensorial artificial viscosity (25) is preferred for accuracy reasons.

The difference between (21) and (24) admits the following flux decomposition

$$\dot{F}_{ij} = m_{ij}\left(\frac{\mathrm{d}U_i}{\mathrm{d}t} - \frac{\mathrm{d}U_j}{\mathrm{d}t}\right) + D_{ij}(U_i - U_j). \tag{27}$$

The raw antidiffusive fluxes for the FCT solution update (2) are given by $F_{ij} = \Delta t\dot{F}_{ij}$, where Δt is the time step and $\dot{F}_{ij}$ is a suitable approximation to

(27). In the predictor-corrector FCT algorithm proposed by Kuzmin [9], the so-defined fluxes F_{ij} are evaluated using the final low-order solution U^L. In particular, the time derivatives at nodes i and j are approximated with (24).

Both explicit and implicit time discretizations of the low-order problem are feasible. In either case, the numerical solution process involves three steps:

- computation of the low-order predictor U^L and assembly of F_{ij};
- synchronized flux limiting in terms of selected primitive variables;
- failsafe postprocessing if undershoots or overshoots are detected.

Many practical aspects (matrix assembly, defect correction, weak imposition of characterictic boundary conditions) of developing an unstructured mesh finite element code for systems of conservation laws are addressed in [7,12].

7 Numerical examples: the Euler equations

In this section, we solve the equations of gas dynamics with the new failsafe FCT algorithm making use of primitive variables. The difference between the reference solution u and a numerical approximation u_h is measured by

$$E_1 = \sum_i m_i |u(x_i, y_i) - u_i| \approx \int_\Omega |u - u_h| \, \mathrm{d}x = ||u - u_h||_1, \tag{28}$$

$$E_2 = \sqrt{\sum_i m_i |u(x_i, y_i) - u_i|^2} \approx \sqrt{\int_\Omega |u - u_h|^2 \, \mathrm{d}x} = ||u - u_h||_2. \tag{29}$$

As before, m_i denotes the i-th diagonal entry of the lumped mass matrix M_L.

7.1 Shock tube problem

Sod's shock tube problem [21] is a standard benchmark for the one-dimensional Euler equations. It models the flow of an inviscid gas in a tube initially separated by a membrane into two sections. Reflective boundary conditions are prescribed at the endpoints of the domain $\Omega = (0, 1)$. The initial condition for the nonlinear Riemann problem is given in terms of the primitive variables

$$\begin{bmatrix} \rho_L \\ v_L \\ p_L \end{bmatrix} = \begin{bmatrix} 1.0 \\ 0.0 \\ 1.0 \end{bmatrix}, \qquad \begin{bmatrix} \rho_R \\ v_R \\ p_R \end{bmatrix} = \begin{bmatrix} 0.125 \\ 0.0 \\ 0.15 \end{bmatrix}, \tag{30}$$

where the subscripts refer to the subdomains $\Omega_L = (0, 0.5)$ and $\Omega_R = (0.5.1)$.

The numerical solutions displayed in Fig. 1 were calculated with an explicit FEM-FCT algorithm on a uniform mesh of 50 linear finite elements. In this example, we use tensorial artificial viscosity (25) and $N = 4$ failsafe correction cycles in which the nodal values of the velocity and pressure are controlled. All simulations are performed with the time step $\Delta t = 10^{-3}$ until the final time $T = 0.231$. The maximum CFL number based on the fastest wave speed $v + c$ is $\nu_{\max} \approx 0.1$. The error norms for each solution are listed in Table 1 (the letters in the first column refer to the corresponding diagrams in Fig. 1).

The objective of this numerical study is to evaluate the performance of the ('unsafe') primitive variable FCT limiter and of the new failsafe feature for several definitions of the synchronized correction factors α_{ij}. The low-order solution ($\alpha_{ij} = 0$) is shown in Fig. 1(a). As expected, it is the most diffusive one. The snapshot in Fig. 1(b) was calculated with the failsafe corrector applied to the unconstrained antidiffusive fluxes ($\alpha_{ij} = 1$). In all other diagrams, the synchronized FCT limiter was applied to the control variables listed in parenthesis. It can readily be seen that the simultaneous control of all primitive variables is required to suppress undershoots and overshoots in the unsafe mode. This option is labeled with $\alpha_{ij}(\rho, p, v)$. Failsafe postprocessing makes it possible to obtain essentially the same results with $\alpha_{ij}(\rho, p)$ or $\alpha_{ij}(\rho)$.

Even the complete deactivation of the main limiter did not cause a major loss of accuracy in this particular test. However, this practice is not generally recommended since it might trigger aggressive limiting at the postprocessing step. In our experience, limiting the pressure and/or density is optimal in the context of synchronous FCT algorithms equipped with the failsafe feature.

Table 1
Shock tube problem: $h = 1/50,\ \Delta t = 10^{-3},\ T = 0.231.$

	ρ		v		p	
	E_1	E_2	E_1	E_2	E_1	E_2
(a)	3.4971e-2	1.9025e-3	7.4816e-2	1.8937e-2	3.4758e-2	2.4455e-3
(b)	1.5667e-2	6.0147e-4	2.6265e-2	5.5811e-3	1.2253e-2	5.0484e-4
(c)	2.9107e-2	2.4776e-3	6.3898e-2	1.9044e-2	2.7097e-2	2.3422e-3
(d)	1.5763e-2	6.1922e-4	2.6190e-2	5.5647e-3	1.2242e-2	5.0479e-4
(e)	2.3217e-2	1.3200e-3	4.2814e-2	9.6829e-3	1.9135e-2	1.1170e-3
(f)	1.5814e-2	6.2411e-4	2.6237e-2	5.6000e-3	1.2250e-2	5.0639e-4
(g)	1.5496e-2	6.0060e-4	2.6175e-2	5.5477e-3	1.2262e-2	5.0672e-4
(h)	1.5493e-2	6.0069e-4	2.6176e-2	5.5471e-3	1.2262e-2	5.0667e-4

(a) Low order, $\alpha_{ij} = 0$

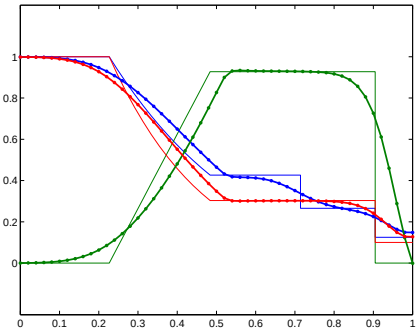

(b) Failsafe FCT, $\alpha_{ij} = 1$

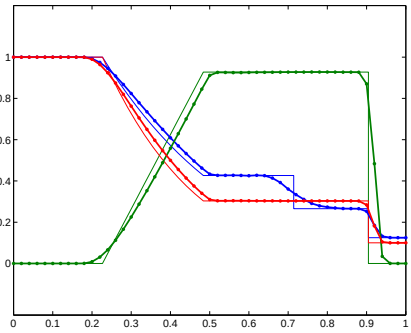

(c) Unsafe FCT, $\alpha_{ij}(\rho)$

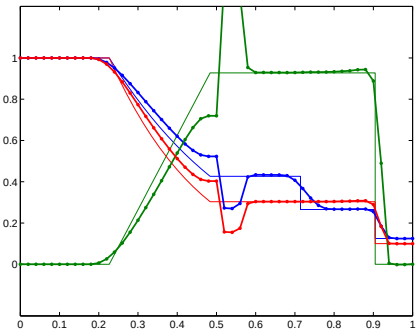

(d) Failsafe FCT, $\alpha_{ij}(\rho)$

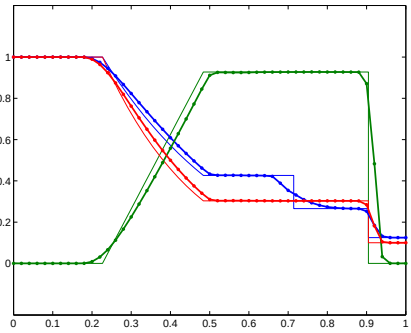

(e) Unsafe FCT, $\alpha_{ij}(\rho, p)$

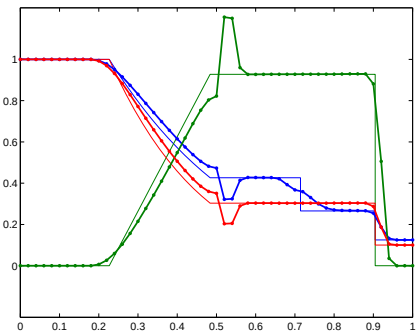

(f) Failsafe FCT, $\alpha_{ij}(\rho, p)$

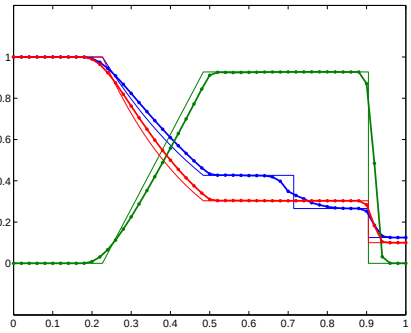

(g) Unsafe FCT $\alpha_{ij}(\rho, p, v)$

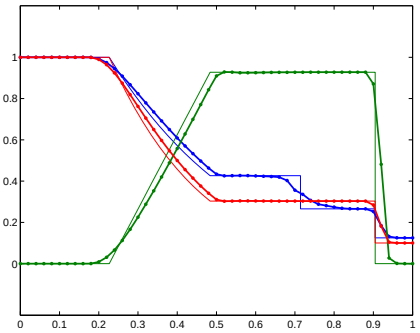

(h) Failsafe FCT, $\alpha_{ij}(\rho, p, v)$

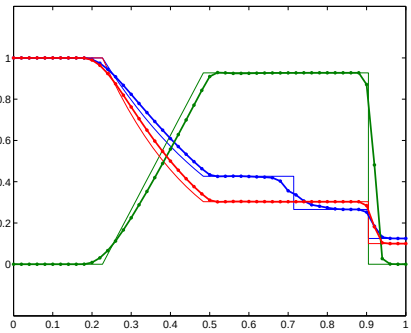

Fig. 1. Shock tube problem: $h = 1/50,\ \Delta t = 10^{-3}$. Snapshots of the density (blue), velocity (green), and pressure (red) distribution at the final time $T = 0.231$.

7.2 Blast wave problem

The blast wave problem of Woodward and Colella [24] is a far more challenging test. The flow of a gamma-law gas, with $\gamma = 1.4$, takes place between reflecting walls, and the initial condition consists of the three constant states

$$\begin{bmatrix} \rho_L \\ v_L \\ p_L \end{bmatrix} = \begin{bmatrix} 1.0 \\ 0.0 \\ 1000.0 \end{bmatrix}, \qquad \begin{bmatrix} \rho_M \\ v_M \\ p_M \end{bmatrix} = \begin{bmatrix} 1.0 \\ 0.0 \\ 0.01 \end{bmatrix}, \qquad \begin{bmatrix} \rho_R \\ v_R \\ p_R \end{bmatrix} = \begin{bmatrix} 1.0 \\ 0.0 \\ 100.0 \end{bmatrix} \tag{31}$$

associated with $\Omega_L = (0, 0.1)$, $\Omega_M = (0.1, 0.9)$, and $\Omega_R = (0.9, 1)$, respectively.

The above initial conditions give rise to two strong blast waves which eventually collide. The flow evolution involves complex interactions of shocks, rarefactions, and contact discontinuities in a small region of space. These interactions are particularly difficult to capture with FCT because of its tendency to clip peaks and distort steep fronts. The latter phenomenon is known as *terracing*. It can be alleviated by means of prelimiting and/or by increasing the phase accuracy of the high-order scheme [26]. In the FEM-FCT context, this means that the flux F_{ij} must contain the contribution of the consistent mass matrix.

Figure 2 displays the density distribution at the final time $T = 0.038$. The numerical algorithm is the same as in the first example. The mesh size and time step are given by $h = 1/400$ and $\Delta t = 10^{-5}$, respectively. The reference solution is calculated numerically on a finer mesh ($h = 10^{-4}$). Again, failsafe postprocessing eliminates the need for limiting all primitive variables, which makes computations more efficient. The results obtained with $\alpha_{ij}(\rho)$ are comparable to those for $\alpha_{ij}(\rho, p, v)$ and much more accurate than the low-order solution in Fig. 2(a). The error norms for all solutions are listed in Table 2. The maximum CFL number for this set of experiments was $\nu_{\max} \approx 33$.

Table 2
Blast wave problem: $h = 1/400,\ \Delta t = 10^{-5},\ T = 0.038$.

	ρ		v		p	
	E_1	E_2	E_1	E_2	E_1	E_2
(a)	2.8905e-1	3.6639e-1	3.9771e-1	5.3052e-1	9.4564e0	4.3774e+2
(b)	1.8334e-1	1.8413e-1	3.0686e-1	9.9360e-1	4.4396e0	1.3128e+2
(c)	1.6059e-1	1.5756e-1	2.7194e-1	8.3193e-1	3.9085e0	1.1485e+2
(d)	1.6305e-1	1.6139e-1	2.7237e-1	8.5377e-1	4.0076e0	1.2024e+2

(a) Low order, $\alpha_{ij} = 0$ (b) Failsafe FCT, $\alpha_{ij}(\rho)$

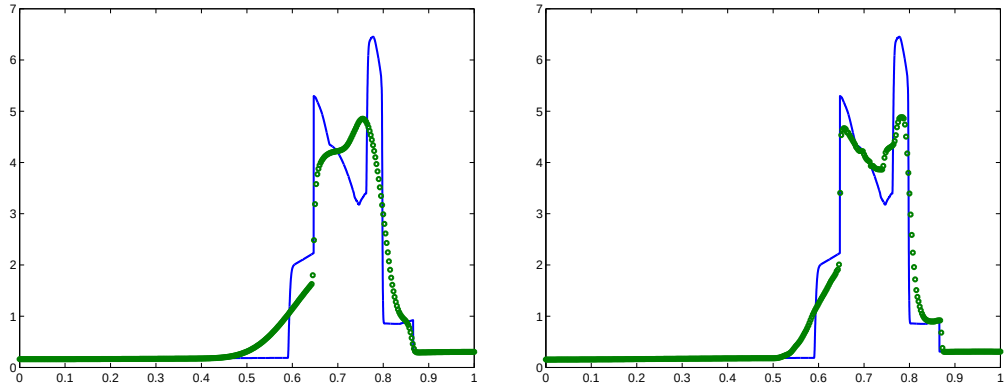

(c) Unsafe FCT $\alpha_{ij}(\rho, p, v)$ (d) Failsafe FCT, $\alpha_{ij}(\rho, p, v)$

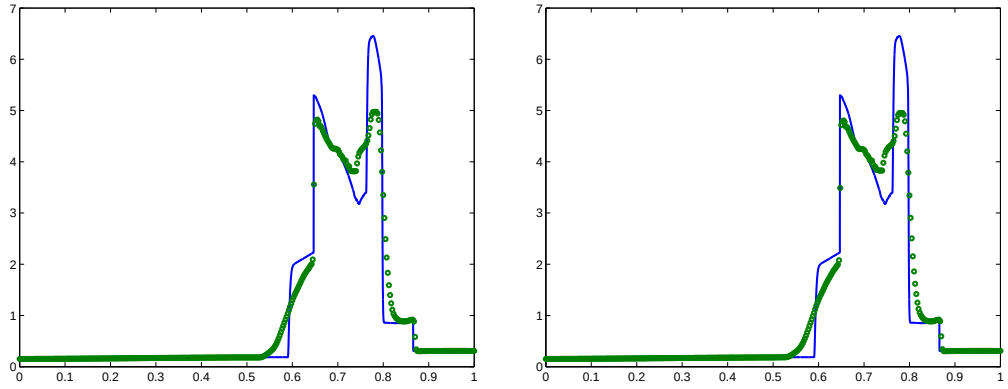

Fig. 2. Blast wave problem: $h = 1/400$, $\Delta t = 10^{-5}$. Snapshots of the density distribution (solid line: reference, bullets: numerical) at the final time $T = 0.038$.

7.3 Double Mach reflection

Another challenging test problem was devised by Woodward and Colella [24] for the two-dimensional Euler equations. The flow pattern involves a Mach 10 shock in air ($\gamma = 1.4$) which initially makes a 60° angle with a reflecting wall.

The computational domain for the double Mach reflection problem is the rectangle $\Omega = (0, 4) \times (0, 1)$. The following pre-shock and post-shock values of the flow variables are used to define the initial and boundary conditions [1]

$$\begin{bmatrix} \rho_L \\ u_L \\ v_L \\ p_L \end{bmatrix} = \begin{bmatrix} 8.0 \\ 8.25\cos(30°) \\ -8.25\sin(30°) \\ 116.5 \end{bmatrix}, \qquad \begin{bmatrix} \rho_R \\ u_R \\ v_R \\ p_R \end{bmatrix} = \begin{bmatrix} 1.4 \\ 0.0 \\ 0.0 \\ 1.0 \end{bmatrix}. \tag{32}$$

Initially, the post-shock values (subscript L) are prescribed in the subdomain $\Omega_L = \{(x,y) \mid x < 1/6 + y/\sqrt{3}\}$ and the pre-shock values (subscript R) in $\Omega_R = \Omega \backslash \Omega_L$. The reflecting wall corresponds to $1/6 \le x \le 4$ and $y = 0$. No boundary conditions are required along the line $x = 4$. On the rest of the boundary, the post-shock conditions are assigned for $x < 1/6 + (1 + 20t)/\sqrt{3}$ and the pre-shock conditions elsewhere [1]. The so-defined values along the top boundary describe the exact motion of the initial Mach 10 shock.

The numerical solutions depicted in Figs. 3–6 were computed with the 2D version of the FCT algorithms from the previous examples. Bilinear finite elements were employed on two structured meshes with equidistant grid spacings $h = 1/64$ and $1/128$. Integration in time was performed until $T = 0.2$ by the Crank-Nicolson time stepping scheme with the time step $\Delta t = 64h \cdot 10^{-4}$.

In all tests, tensorial artificial viscosity was used to calculate the low-order solution which is displayed in Figs. 3–4 (a). Due to strong numerical diffusion, the complex interplay of incident, reflected, and Mach stem shock waves is resolved rather poorly, and so is the slipstream at the triple point. Remarkably, all FCT schemes under investigation succeed in capturing the weak Mach shock that emanates from the second triple point and dies as soon as it reaches the slipstream. In preliminary computations by the FCT algorithm in which the x- and y-velocities were constrained individually, the curled slipstream was found to catch up with the leading Mach stem, giving rise to an unphysical kink. For this reason, using the weighted average (15) of velocity correction factors is essential if the velocity belongs to the set of control variables.

The snapshots in Figs. 3–4 (d) were calculated with the failsafe corrector applied to the unconstrained antidiffusive fluxes ($\alpha_{ij} = 1$). The local bounds for **all** primitive variables – density, pressure and velocity – were controlled in this case. The numerical results in Figs. 3–4 (e) were obtained with the algorithm in which Zalesak's limiter is applied to the density field, whereas the velocity and pressure bounds are enforced via failsafe postprocessing. For this particular problem, a posteriori control of the velocity and pressure is a must if $\mathbf{v}$ and p are not constrained by the FCT limiter. The simulation crashes immediately if the $\alpha_{ij}(\rho)$ version is used without the failsafe feature.

For better visualization of small-scale effects, we also present the numerical Schlieren diagrams that represent gray-scale images of the scalar quantity [2]

$$\sigma = \exp\left\{-\beta\left(\frac{|\nabla\rho| - \min|\nabla\rho|}{\max|\nabla\rho| - \min|\nabla\rho|}\right)\right\},$$

where the smallest and largest magnitude of the density gradient are computed over the entire domain, and the exposure value is $\beta = 15$. The Schlieren images depicted in Figs. 5–6 are quite helpful in visualizing small details which cannot be represented by contour lines. The excess amount of numerical dissipation

(a) Low-order, $\alpha_{ij} = 0$

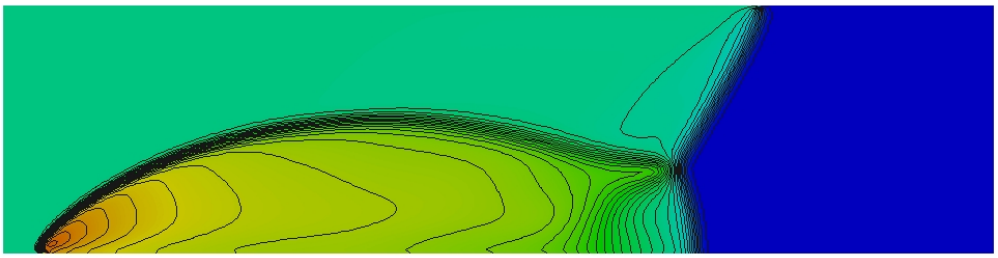

(b) Unsafe FCT, $\alpha_{ij}(\rho, p)$

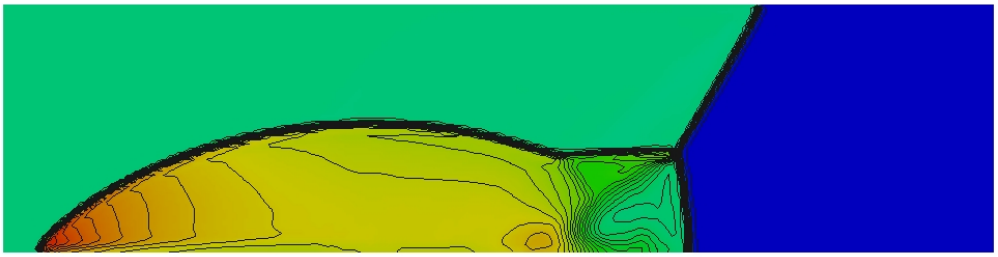

(c) Unsafe FCT, $\alpha_{ij}(\rho, p, \mathbf{v})$

(d) Failsafe FCT, $\alpha_{ij} = 1$

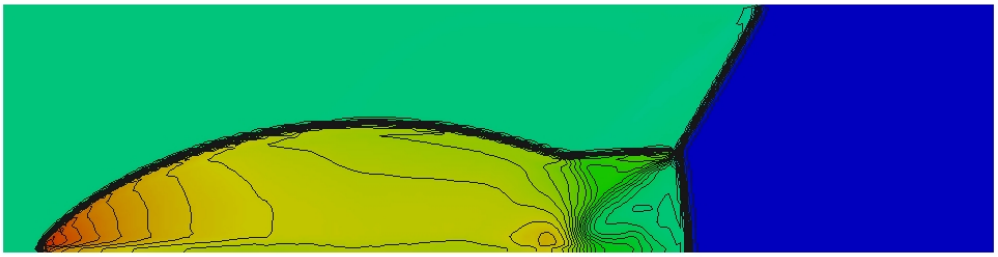

(e) Failsafe FCT, $\alpha_{ij}(\rho)$

Fig. 3. Double Mach reflection: 16,384 Q_1 elements, $T = 0.2$.

(a) Low-order, $\alpha_{ij} = 0$

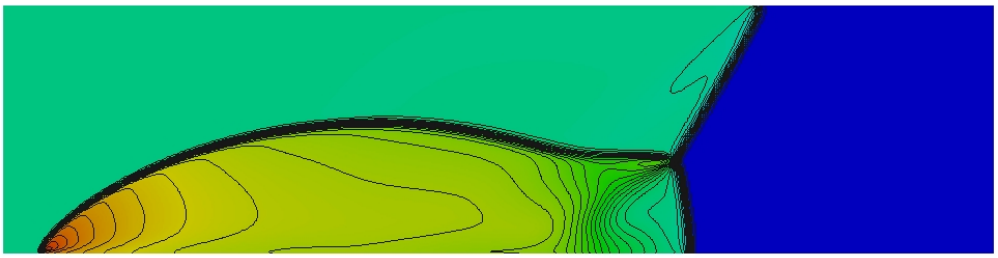

(b) Unsafe FCT, $\alpha_{ij}(\rho, p)$

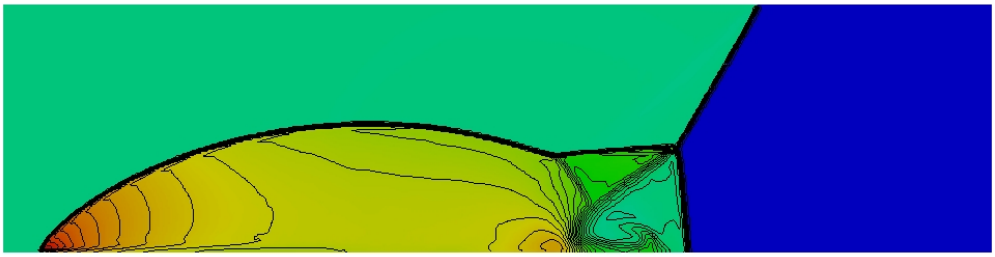

(c) Unsafe FCT, $\alpha_{ij}(\rho, p, \mathbf{v})$

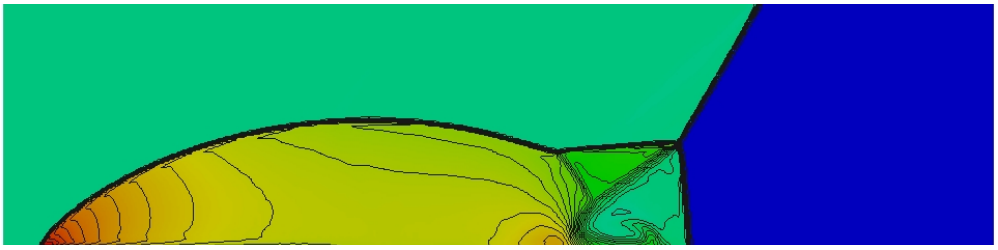

(d) Failsafe FCT, $\alpha_{ij} = 1$

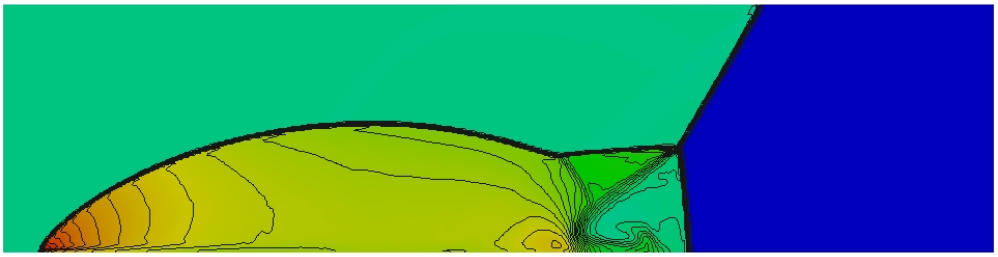

(e) Failsafe FCT, $\alpha_{ij}(\rho)$

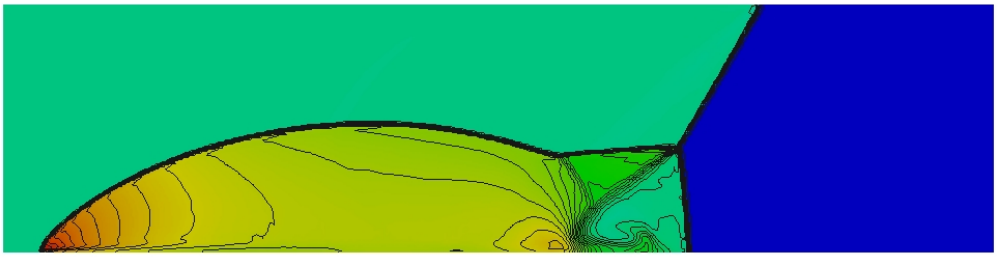

Fig. 4. Double Mach reflection: 65,536 Q_1 elements, $T = 0.2$.

(a) Low-order, $\alpha_{ij} = 0$

(b) Unsafe FCT, $\alpha_{ij}(\rho, p)$

(c) Unsafe FCT, $\alpha_{ij}(\rho, p, \mathbf{v})$

(d) Failsafe FCT, $\alpha_{ij} = 1$

(e) Failsafe FCT, $\alpha_{ij}(\rho)$

Fig. 5. Double Mach reflection: 16,384 Q_1 elements, $T = 0.2$.

(a) Low-order, $\alpha_{ij} = 0$

(b) Unsafe FCT, $\alpha_{ij}(\rho, p)$

(c) Unsafe FCT, $\alpha_{ij}(\rho, p, \mathbf{v})$

(d) Failsafe FCT, $\alpha_{ij} = 1$

(e) Failsafe FCT, $\alpha_{ij}(\rho)$

Fig. 6. Double Mach reflection: 65,536 Q_1 elements, $T = 0.2$.

Unsafe FCT, $\alpha_{ij}(\rho, p)$

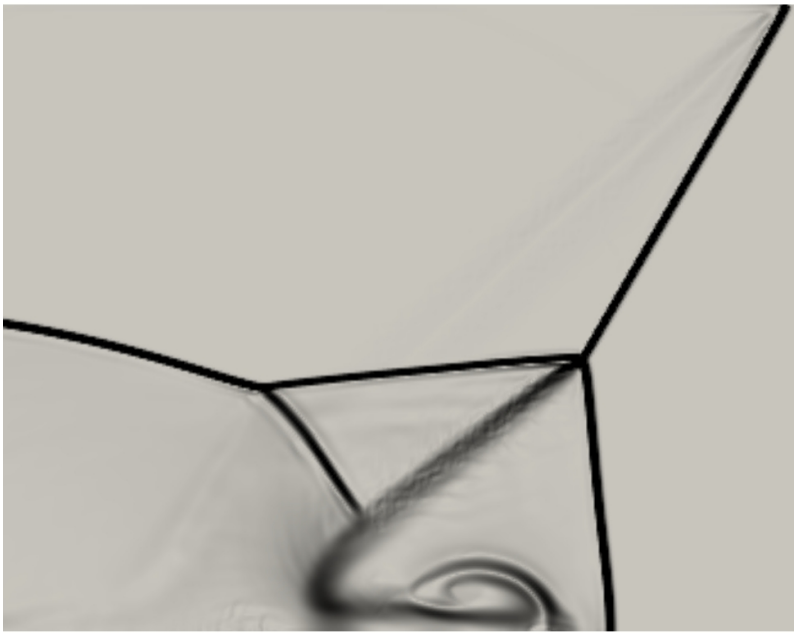

Fig. 7. Double Mach reflection: 262,144 Q_1 elements, $T = 0.2$.

inherent to the low-order scheme is illustrated by the thickness of the waves and the lack of small scale features in Figs. 5–6 (a). In contrast, the resolution of the numerical results produced by flux correction with and without the new failsafe feature are equally crisp. The close-up diagram in Fig. 7 indicates that the complex wave pattern in the vicinity of the triple points is resolved with high precision. The numerical solution was computed on a very fine mesh with equidistant grid spacing $h = 1/256$ using the time step size $\Delta t = 2.5 \cdot 10^{-5}$.

8 Case study: constrained interpolation

Another task that calls for the use of failsafe flux limiting is the projection (initialization, interpolation, postprocessing) of data in conservative numerical algorithms for the equations of fluid dynamics. If the initial data are prescribed analytically, it is essential to guarantee that the numerical solution has the same total mass, momentum, and energy when the simulation begins. Moreover, undershoots and overshoots are to be avoided. In a similar vein, the interpolation of data after adaptive remeshing or mesh coarsening should be conservative and bounded. Shashkov et al. [13,17,20] developed such interpolation techniques for a class of Arbitrary Lagrangian Eulerian (ALE) methods that require rezoning and remapping. One of the most recent advances in this area is the synchronized Flux-Corrected Remapping (FCR) algorithm [13] in which the density and velocity fields are constrained in a coupled manner.

Löhner ([14], pp. 257–260) presents a conservative and monotonic interpolation technique in which the FCT limiter is applied to the difference between the consistent and lumped-mass L^2 projections. The latter serves as the low-order method that satisfies the maximum principle for linear finite elements [5]. Again, the purpose of flux correction is to guarantee that the projected solution is bounded by the local maxima and minima of the low-order predictor.

The present paper focuses on synchronized FCT remapping for systems of conserved variables. Let U denote the initial data or numerical solution from a different finite element space. The standard L^2 projection is defined by

$$\int_\Omega W_h U_h^H \, \mathrm{d}\mathbf{x} = \int_\Omega W_h U \, \mathrm{d}\mathbf{x}, \qquad \forall W_h, \tag{33}$$

where U_h^H is the consistent Galerkin approximation and $W_h \in \{\varphi_i\}$ is a test function defined on the current mesh. The lumped-mass approximation

$$\int_\Omega U_h^L \, \mathrm{d}\mathbf{x} = \int_\Omega W_h U \, \mathrm{d}\mathbf{x}, \qquad \forall W_h \tag{34}$$

yields a low-order predictor U_h^L which has the same 'mass' as U_h^H but is free of undershoots/overshoots, at least in the case of linear finite elements [5].

Note that the right-hand sides of (33) and (34) are the same. If the functions W_h and U are defined on different meshes, numerical integration can be performed using a *supermesh* that represents the union of the two meshes [5]. The computation of U^H involves solving a linear system of the form

$$M_C U^H = R,$$

where $M_C = \{m_{ij}\}$ is the consistent mass matrix and R is the load vector with components $R_i = \int_\Omega \varphi_i U \, \mathrm{d}\mathbf{x}$. The low-order solution is given by

$$M_L U^L = R,$$

where M_L is the diagonal counterpart of M_C. As before, the entries of the two mass matrices are related by (23). The high-order system can be solved efficiently using the Richardson iteration method preconditioned by M_L

$$M_L U^{(m+1)} = R + (M_L - M_C) U^{(m)}, \quad m = 0, 1, \ldots. \tag{35}$$

Since the matrix M_C is diagonally dominant and well-conditioned, 3–5 iterations are enough. A usable initial guess is the low-order solution $U^{(0)} = U^L$.

By construction, the difference between the nodal values of the functions U_h^H and U_h^L admits a conservative flux decomposition of the form (2) with

$$F_{ij} = m_{ij}(U_i^H - U_j^H). \tag{36}$$

The process of flux limiting involves the same algorithmic steps as the above FEM-FCT scheme for the Euler equations. The nodal values of the projected solution are given by (4), where the synchronized correction factors α_{ij} are calculated with Zalesak's limiter. The use of the failsafe feature is optional.

9 Numerical examples: constrained interpolation

In this section, we present a numerical study of the synchronized FCT limiter as a tool for constraining the Galerkin L^2 projection of discontinuous data. In the examples that follow, there was no need for the failsafe corrector because no undershoots/overshoots were found in the velocity and pressure fields.

9.1 Constrained initialization

The initialization process is rarely described in publications on numerical methods for fluid flows. The simple pointwise definition of nodal values

$$U_i^0 = U_0(\mathbf{x}_i) \tag{37}$$

is generally nonconservative. This may result in significant errors if the computational mesh is too coarse in regions where the function U_0 is discontinuous.

The Galerkin L^2 projection (33) with $U = U_0$ is conservative but not monotone. On the other hand, the lumped-mass version (34) is less accurate for smooth data. This is the rationale for the use of the proposed FCT limiter.

As a model problem, consider a subdivision of $\Omega = (0,1)^2$ into M triangular or quadrilateral elements Ω_e and prescribe the radially symmetric profile

$$\rho = \begin{cases} 1.0 & \text{if} \quad 0.3 \le r \le 0.4, \\ 0.01 & \text{otherwise,} \end{cases} \qquad \mathbf{v} = \begin{bmatrix} 0.0 \\ 0.0 \end{bmatrix}, \qquad p = 1,$$

where $r = \sqrt{(0.5-x)^2 + (0.5-y)^2}$. Since the density field is discontinuous, adaptive cubature formulas [23] are employed to evaluate the integral

$$R_i^\rho = \int_\Omega \varphi_i \rho \, \mathrm{d}\mathbf{x} = \sum_{e=1}^{M} \int_{\Omega_e} \varphi_i \rho \, \mathrm{d}\mathbf{x} = \sum_{e=1}^{M} \sum_{s=0}^{4^l} \int_{\omega_s} \varphi_i \rho \, \mathrm{d}\mathbf{x},$$

where $l = 0, 1, 2, \ldots$ is the refinement level for numerical integration. That is, each cell Ω_e is subdivided into 4^l triangles or quadrilaterals. Then a standard cubature formula, e.g. the 3-point Gauss rule for linear and the 3×3 Gauss formula for bilinear elements, is applied on each subelement ω_s. Adaptive quadrature rules can be equipped with error control strategies that determine the 'optimal' refinement level individually for each element [23]. In the numerical examples presented below, the fixed value $l = 4$ was employed.

The density profiles shown in Fig. 8 (a-c) were obtained using linear (left) and bilinear (right) finite element projections onto uniform meshes with spacing $h = 1/32$. As expected, the consistent L^2 projection fails to preserve the bounds of the initial data $0.01 \leq \rho_0 \leq 1.0$, while its lumped-mass counterpart gives rise to significant numerical diffusion. The synchronized FCT limiter with $\alpha_{ij} = \alpha_{ij}^\rho$ makes it possible to achieve crisp resolution of the discontinuous initial profile without generating undershoots or overshoots, see Fig. 8 (c).

The global maxima and minima of ρ_h, as well as the L^2 norms of the difference between the exact solution and each approximation, are listed in Tables 3–4. The consistent L^2 projection yields the smallest overall error but exceeds the theoretical upper bound by almost 10% and produces negative densities. The largest L^2 error is observed for the lumped-mass projection. The FEM-FCT solution is more accurate, and its nodal values lie in the same range. The row that begins with (*) corresponds to evaluation of the raw antidiffusive fluxes $F_{ij} = m_{ij}(U_i^L - U_j^L)$ using the low-order nodal values. This approximate FCT projection is slightly more diffusive than the algorithm based on (36). The results shown in the last row were obtained with pointwise initialization (37) which does not preserve the exact total mass $\int_\Omega \rho \, \mathrm{d}\mathbf{x} = 2.2771237\text{e-}1$.

Table 3
Constrained initialization: bilinear finite elements.

	ρ				
	$\int_\Omega \rho_h \, \mathrm{d}\mathbf{x}$	$\|\rho - \rho_h\|_1$	$\|\rho - \rho_h\|_2$	$\min(\rho_h)$	$\max(\rho_h)$
(a)	2.277e-1	5.0101e-2	1.1296e-1	-1.8779e-1	1.2118
(b)	2.277e-1	6.2709e-2	1.3568e-1	1.0000e-2	1.0000
(c)	2.277e-1	5.2544e-2	1.2519e-1	1.0000e-2	1.0000
(*)	2.277e-1	5.2181e-2	1.2589e-1	1.0000e-2	1.0000
(**)	2.188e-1	4.3021e-2	1.3064e-1	1.0000e-2	1.0000

Table 4
Constrained initialization: linear finite elements.

	ρ				
	$\int_\Omega \rho_h \, \mathrm{d}\mathbf{x}$	$\|\rho - \rho_h\|_1$	$\|\rho - \rho_h\|_2$	$\min(\rho_h)$	$\max(\rho_h)$
(a)	2.277e-1	4.0545e-2	1.0031e-1	-2.2515e-1	1.2006
(b)	2.277e-1	4.5721e-2	1.1679e-1	1.0000e-2	1.0000
(c)	2.277e-1	3.9665e-2	1.1002e-1	1.0000e-2	1.0000
(*)	2.277e-1	3.9353e-2	1.1027e-1	1.0000e-2	1.0000
(**)	2.303e-1	3.2174e-2	1.1883e-1	1.0000e-2	1.0000

(a) consistent L^2 projection, $\alpha_{ij} = 1$

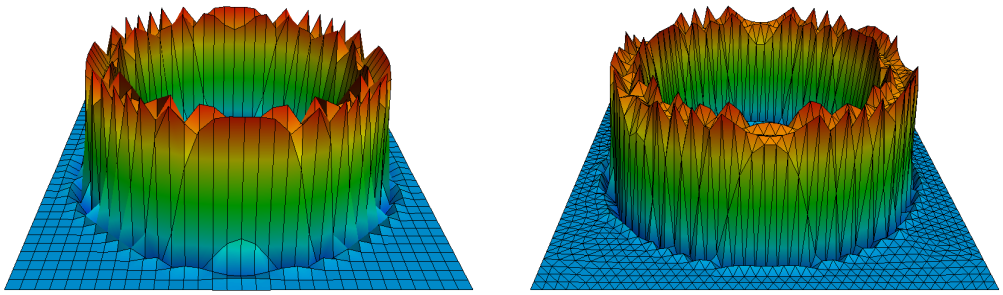

(b) mass-lumped L^2 projection, $\alpha_{ij} = 0$

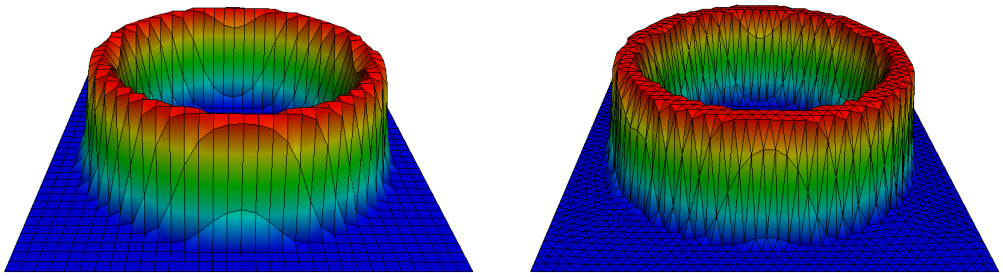

(c) constrained L^2 projection, $\alpha_{ij}(\rho)$

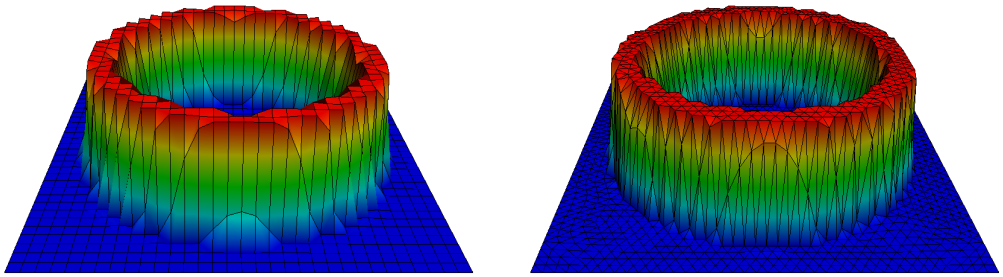

Fig. 8. Constrained initialization: linear *vs.* bilinear finite elements.

In many applications, the data to be projected represent numerical solutions calculated on a different mesh or using another set of basis functions. The transfer of information from one space to another is an integral part of adaptive finite element methods. The need for conservative and bounded interpolation arises whenever mesh coarsening, remeshing, or rezoning are performed.

To assess the accuracy of our FEM-FCT projection scheme in the context of constrained interpolation, we triangulate the square domain $\Omega = (0,1)^2$ as shown in Fig. 9 (a) and prescribe the following solution values

$$\rho_i = \begin{cases} 1.0 & \text{if} \quad 0.3 \le r_i, \\ 0.01 & \text{otherwise}, \end{cases} \qquad \mathbf{v}_i = \begin{bmatrix} 0.0 \\ 0.0 \end{bmatrix}, \qquad p_i = 1$$

at the vertices of the unstructured mesh. As in the previous example, r_i measures the distance from the center $(x_0, y_0) = (0.5, 0.5)$. The background mesh is constructed in such a way that a number of grid points lie on the circle of radius $r = 0.3$ where the density ρ is discontinuous, see Fig. 10 (a).

The consistent, lumped, and constrained L^2 projection schemes are employed to transfer the above solution onto the generalized tensor product mesh shown in Fig. 9 (b). This mesh is constructed by regular refinement of a quadrilateral 3×3 grid whose inner points are displaced in a nonsymmetric fashion. The interpolated solution profiles are depicted in Fig. 10 (b–d). The consistent L^2 projection produces overshoots and undershoots of about 8.5%. In contrast, the nodal values obtained with the lumped-mass L^2 projection and FEM-FCT vary between 0.01 and 1.0, as desired. The high accuracy of constrained interpolation is clearly visible from the error norms presented in Table 5. The last row shows the results for the approximate FCT projection scheme in which the raw antidiffusive fluxes F_{ij} are evaluated using U^L instead of U^H.

In this test, the smallest L^2 error is obtained with the lumped-mass version but this does not imply that the FCT correction is useless. On a given coarse mesh, a high-order solution is not guaranteed to be more accurate than a low-order one. However, the errors decrease faster when the mesh becomes sufficiently fine. Thus, a direct comparison of errors measured in a global norms can be misleading. What really matters is the asymptotic rate of convergence.

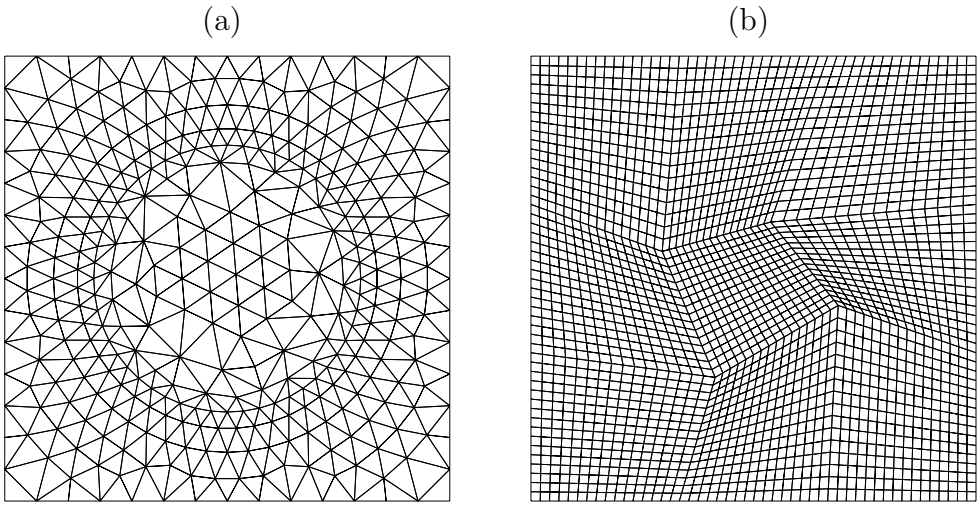

Fig. 9. Constrained interpolation: original (a) and target (b) meshes.

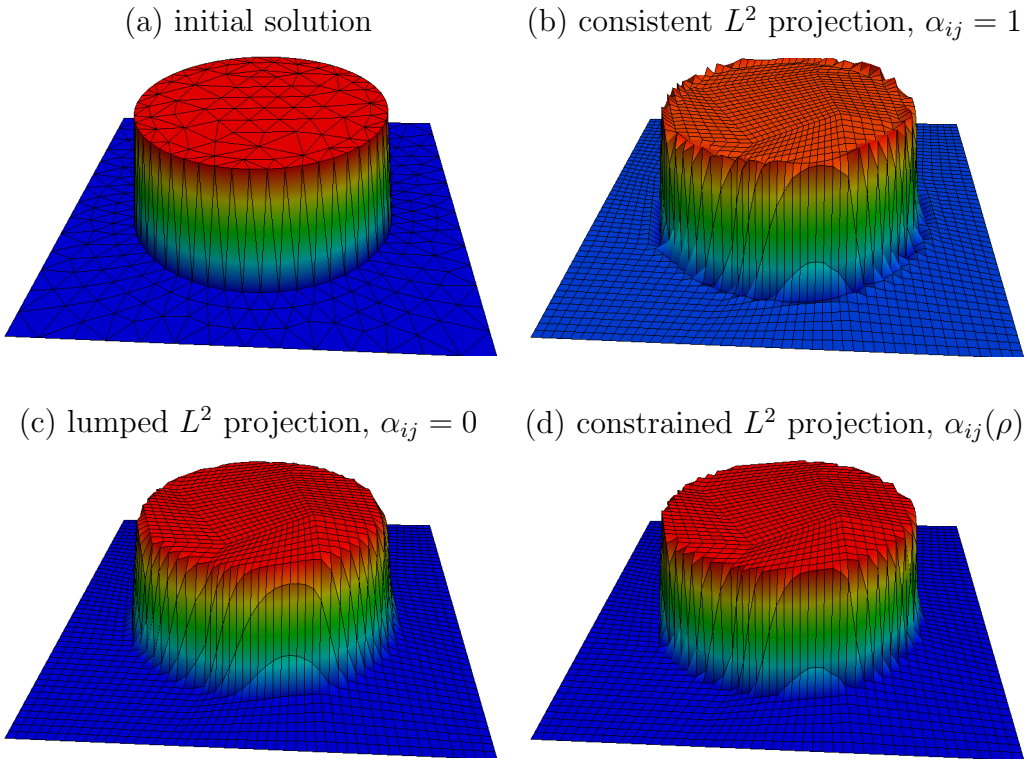

Fig. 10. Constrained interpolation: initial and interpolated solutions.

10 Conclusions

This paper sheds some light on the aspects of flux correction for systems of conservation laws. A new approach to constraining the primitive variables in

Table 5
Constrained interpolation: mass conservation and error norms.

	ρ				
	$\int_\Omega \rho_h \, \mathrm{d}\mathbf{x}$	$\|\rho - \rho_h\|_1$	$\|\rho - \rho_h\|_2$	$\min(\rho_h)$	$\max(\rho_h)$
(a)	3.2535e-1	2.6026e-2	1.1693e-1	0.1000e-1	1.0000
(b)	3.2535e-1	3.8066e-2	1.5126e-1	-0.6979e-1	1.0850
(c)	3.2535e-1	4.0346e-2	1.4399e-1	0.1000e-1	1.0000
(d)	3.2535e-1	3.7100e-2	1.5015e-1	0.1000e-1	1.0000
(*)	3.2535e-1	3.7459e-2	1.4831e-1	0.1000e-1	1.0000

synchronized FCT algorithms is proposed. It differs from other flux limiters for systems in that the transformation of variables is performed node-by-node rather than edge-by-edge. Furthermore, the robustness of the generalized Zalesak limiter is reinforced by means of a simple failsafe corrector designed to preserve the bounds of the low-order solution. A numerical study is performed to illustrate the practical utility of the proposed methodology in the context of finite element flow solvers and conservative data projections. The results indicate that the cost of flux limiting can be significantly reduced, e.g., using FCT to constrain the pressure and/or density only. In this case, the failsafe feature provides an inexpensive way to fix the final solution whenever undershoots/overshoots are detected. In conclusion, the design of FCT algorithms for the equations of fluid dynamics requires (i) a careful choice of the variables to be controlled, (ii) a suitable synchronization of the correction factors, and (iii) a mechanism that makes it possible to 'undo' the antidiffusive correction whenever it turns out to be harmful. We believe that all of these ingredients are important when it comes to solving compressible flow problems using FCT.

Acknowledgements

This research was supported by the German Research Association (DFG) under grant KU 1530/3-1 and within the framework of SFB 708.

References

[1] Athena test suite, `http://www.astro.virginia.edu/VITA/ATHENA/dmr.html`.

[2] J.W. Banks, W.D. Henshaw, and J.N. Shadid, An evaluation of the FCT method for high-speed flows on structured overlapping grids. J. Comput. Phys. 228 (2009) 5349–5369.

[3] J. P. Boris and D. L. Book, Flux-corrected transport. I. SHASTA, A fluid transport algorithm that works. J. Comput. Phys. 11 (1973) 38–69.

[4] C. R. DeVore, An improved limiter for multidimensional flux-corrected transport, NASA Technical Report, AD-A360122 (1998).

[5] P.E. Farrell, M.D. Piggott, C.C. Pain, G.J. Gorman, and C.R. Wilson, Conservative interpolation between unstructured meshes via supermesh construction. Comput. Methods Appl. Mech. Engrg. 198 (2009) 2632–2642.

[6] C. A. J. Fletcher, The group finite element formulation. Comput. Methods Appl. Mech. Engrg. 37 (1983) 225–243.

[7] M. Gurris, Implicit Finite Element Schemes for Compressible Gas and Particle-Laden Gas Flows. Ph.D. thesis, Dortmund University of Technology, 2010.

[8] C. Hirsch, Numerical Computation of Internal and External Flows. Vol. II: Computational Methods for Inviscid and Viscous Flows. John Wiley & Sons, Chichester, 1990.

[9] D. Kuzmin, Explicit and implicit FEM-FCT algorithms with flux linearization. J. Comput. Phys. 228 (2009) 2517–2534.

[10] D. Kuzmin, M. Möller, and S. Turek, High-resolution FEM-FCT schemes for multidimensional conservation laws. Comput. Methods Appl. Mech. Engrg. 193 (2004) 4915–4946.

[11] D. Kuzmin and M. Möller, Algebraic flux correction I. Scalar conservation laws. In: D. Kuzmin, R. Löhner, S. Turek (eds.), Flux-Corrected Transport: Principles, Algorithms, and Applications, Springer, Berlin, 2005, pp. 155–206.

[12] D. Kuzmin and M. Möller, Algebraic flux correction II. Compressible Euler Equations. In: D. Kuzmin, R. Löhner, S. Turek (eds.), Flux-Corrected Transport: Principles, Algorithms, and Applications, Springer, Berlin, 2005, pp. 207–250.

[13] R. Liska, M. Shashkov, P. Váchal, and B. Wendroff, Optimization-based synchronized Flux-Corrected Conservative interpolation (remapping) of mass and momentum for Arbitrary Lagrangian-Eulerian methods. J. Comput. Phys. 229 (2010) 1467–1497.

[14] R. Löhner, Applied CFD Techniques: An Introduction Based on Finite Element Methods. Second Edition, John Wiley & Sons, 2008.

[15] R. Löhner and J.D. Baum, 30 years of FCT: Status and directions. In: D. Kuzmin, R. Löhner, and S. Turek (eds.), Flux-Corrected Transport: Principles, Algorithms, and Applications. Springer, Berlin, 2005, pp. 131–154.

[16] R. Löhner, K. Morgan, J. Peraire, and M. Vahdati, Finite element flux-corrected transport (FEM-FCT) for the Euler and Navier-Stokes equations. Int. J. Numer. Meth. Fluids, 7 (1987) 1093–1109.

[17] L.G. Margolin and M. Shashkov, Second-order sign-preserving conservative interpolation (remapping) on general grids. J. Comput. Phys. 184 (2003) 266–298.

[18] P. L. Roe, Approximate Riemann solvers, parameter vectors and difference schemes. J. Comput. Phys. 43 (1981) 357–372.

[19] C. Schär and P. K. Smolarkiewicz, A synchronous and iterative flux-correction formalism for coupled transport equations. J. Comput. Phys. 128 (1996) 101–120.

[20] M. Shashkov and B. Wendroff, The repair paradigm and application to conservation laws. J. Comput. Phys. 198 (2004) 265–277.

[21] G. Sod, A survey of several finite difference methods for systems of nonlinear hyperbolic conservation laws. J. Comput. Phys. 27 (1978) 1–31.

[22] P. Váchal and R. Liska, Sequential Flux-Corrected Remapping for ALE Methods. In: A. Bermudez de Castro, D. Gomez, P. Quintela, and P. Salgado (eds.) Numerical Mathematics and Advanced Applications (ENUMATH 2005). Springer, 2006, pp. 671-679.

[23] W. Vogt, Adaptive Verfahren zur numerischen Quadratur und Kubatur. Preprint No. M 1/06, IfMath TU Ilmenau, 2006.

[24] P. R. Woodward, P. Colella, The numerical simulation of two-dimensional fluid flow with strong shocks. J. Comput. Phys. 54 (1984) 115–173.

[25] S. T. Zalesak, Fully multidimensional flux-corrected transport algorithms for fluids. J. Comput. Phys. 31 (1979) 335–362.

[26] S. T. Zalesak, The design of Flux-Corrected Transport (FCT) algorithms for structured grids. In: D. Kuzmin, R. Löhner, S. Turek (eds.), Flux-Corrected Transport: Principles, Algorithms, and Applications, Springer, Berlin, 2005, pp. 29–78.